Softness-driven complexity in supercrystals of gold nanoparticles

Brigitte Pansu, Claire Goldmann, Doru Constantin, Marianne Impéror-Clerc, Jean-François Sadoc

Softness-driven complexity in supercrystals of gold nanoparticles *

Brigitte PANSU,†[a] Claire GOLDMANN,[a], Doru CONSTANTIN [a],
Marianne IMPÉROR -CLERC[a] and Jean-François SADOC [a]

Abstract

Many soft matter systems are composed of roughly spherical objects that can self-assemble in ordered structures. Unlike hard spheres, at high volume fraction these soft spheres adapt their shape to the local geometrical constraints and the question of space filling needs to be entirely revisited. Hydrophobically coated gold nanocrystals self-assemble in supercrystals and are good candidates to explore this question. When the soft coating is thin compared to the rigid core, a FCC structure is obtained, with a behaviour similar to that of hard spheres. In the opposite case, for a thick soft coating, a BCC structure is found instead. This paper focus on the intermediate region between these two classical structures. By varying the gold core radius R and the ligand fully extended length L, we establish a structure diagram based on a large experimental data set. The hexagonal Frank-Kasper C14 structure is observed for various values of R and L and can coexist with a FCC phase. Depending on the structure, values of the minimum thickness e of the ligand shell compared to L are different. These experimental results confirm that the C14 Frank-Kasper phase is a solution to the problem of filling the space with soft particles even with a rigid core and should help to establish pertinent models in order to predict the structures of the superlattices built by gold nanoparticles.

1 Introduction

Understanding how atoms or particles can fill the space is a long standing challenge. When such objects behave like hard spheres, they form compact structures like the face centered cubic (FCC) structure or the hexagonal closed packed (HCP) structure. However hard sphere interaction cannot describe properly most systems. The interaction between atoms or molecules is usually more complex and other structures like the body-centered cubic structure (BCC) are commonly observed even for classical metals. More complex arrangements such as Frank-Kasper phases, or even quasicrystalline structures, are also observed, mainly in alloys[1,2]. Many soft matter systems consist of roughly spherical objects that can self-assemble in ordered structures. Since these soft particles can adapt their shape to the local geometrical constraints, the question of filling the space needs to be entirely revisited. The softness as well as the diversity of interaction in these systems and the role of entropy at the colloidal scale open the route to complex structures. The first ordered structures that have been observed in colloidal crystals are classical stackings such as FCC or BCC[3]. But, in foams, D. Weaire and R. Phelan[4] have shown that a complex structure analogous to the β-tungsten structure (also known as A15, shown in Fig.1a), was a better solution of the "Kelvin problem" (minimization of the surface area) than the previous best candidate (BCC) suggested by Lord Kelvin. The A15 structure is tetrahedrally close-packed (TCP) and belongs to the family of the Frank-Kasper (FK) phases, one of the largest groups of inter-metallic compounds, characterized by a local tetrahedral order that cannot extend uniformly and perfectly to arbitrary long distances. This concept of minimizing interfacial area also applies to the ordered micellar and inverse micellar lyotropic liquid-crystalline phases formed by amphiphilic molecules such as lipids and surfactants[5]. Various non standard cubic structures (A15, C15...) are built by the amphiphilic aggregates, allowed by the interfacial curvature but also by the role of curvature elasticity and packing constraints[6]. Numerous non close-packed crystal structures have been observed at the colloidal scale. To explain this diversity, geometrical considerations must be combined with

*Electronic Supplementary Information (ESI) available. See DOI: 10.1039/D1SM00617G/

†E-mail: brigitte.pansu@universite-paris-saclay.fr

[a] *Université Paris-Saclay, CNRS, Laboratoire de Physique des Solides, 91405, Orsay, France*

thermodynamic energy as well as entropic considerations. For instance, in fuzzy colloids, Ziherl and Kamien[7] have shown that the close-packing rule associated with hard-core interactions and positional entropy of particles is frustrated by a minimum-area principle associated with the soft tail and internal entropy of the soft coronas.

The Frank-Kasper phases are often considered as precursors of quasicrystalline phases. The first quasicrystalline phases in soft matter have been discovered in dendrimers. Dendrons and dendrimers (tree-like molecules) are proving particularly versatile in generating periodic nanostructures. Two cubic micellar lattices (BCC and A15) have been observed as well as a tetragonal phase (σ phase). Playing with temperature has revealed the presence of a quasicrystalline (dodecagonal) phase[8].

Diblock copolymers melts are good candidates[9] to investigate different "'soft" structures since the size and mechanical property of each block can be adjusted. Following the discovery of a FK tetragonal σ phase in a diblock copolymer melt in 2010[10], there has been a renewed interest in the phase behavior of diblock copolymer melts with asymmetric composition, revealing several previously unanticipated structures, including the A15, C14 (Fig.1b) and C15 phases (Fig.1c) in addition to a dodecagonal quasicrystalline phases[11–13]. Frank-Kasper phases, notably the hexagonal Z phase, and quasicrystal phases, as well as their transition sequence, have also been reported in one-component giant surfactants by introducing variations in molecular geometry[14,15]. Frank-Kasper phases have also been observed in aqueous dispersions of colloidal silica[16] with a broad monomodal size distribution (14 % polydispersity, 8 nm size). Over a range of volume fractions, the silica particles segregate and build distinct sets of colloidal crystals. These dispersions demonstrate fractional crystallization and multiple-phase (BCC, C14, liquid) coexistence.

Due to their optical properties, metallic nanoparticles (NPs) have encountered a large interest over the last years. Their stabilization in suspension requires the presence of ligands at their surface, ligands that can be either hydrophobic or hydrophilic. When the NPs are sufficiently monodisperse, they can self assemble in superlattices. In many systems, the observed structures are FCC or BCC, mainly depending on the ratio between the rigid core size and the soft ligand corona thickness. The role of the entropy associated with capping ligand packing frustration in superlattices is essential to understand the appearance of a BCC or FCC structure as shown in[17]. But more complex structures have been revealed first upon heating[18], then on stable structures at room temperature[19]. Due to the presence of different sites (see Fig. 1), Frank-Kasper phases are often observed in binary systems, for classical alloys as well as in soft matter[20–23]. The self-assembly of binary mixtures of two sizes of spherical nanocrystals has revealed a surprisingly diverse library of structures[23]. At least 15 distinct binary nanocrystal superlattice structures have been reported. The soft and deformable layer of ligands grafted on the nanocrystal has been identified as contributing significantly to the overall size and shape of assembling particles. Nevertheless Frank-Kasper phases have been observed for one-size nanocrystals assembly[19] even if, with a 15% polydispersity of the core size, the role of polydispersity remains an opened question as as for other systems.

Indeed, the Frank-Kasper phases can be seen as packing of polyhedra with different volumes and this has to be taken into account in any model. Theoretical analysis[24] has shown the emergence of the optimal relaxation of cellular domains to unequal volumes to simultaneously minimize area and maximize compactness of cells, highlighting an important connection between crystal structures in condensed matter and optimal lattices in discrete geometry. A recent analysis[25] reveals that, when the volume ratio of large polyhedron to small polyhedron ranges from 1.0 to 1.25, the A15 phase has a minimum surface area and a minimum free energy. For the volume ratio $\approx$1.33, a hexagonal Z phase is the structure that minimizes surface contact area. For the volume ratio $\approx$1.5, a C14 or C15 phase is instead preferred.

Complex packings, also encountered for metals and their alloys, have been observed in several soft matter systems suggesting universality in the packing of soft particles, even if the richness in ordering patterns arises from different types of frustration in such systems. In 2015, we reported[19] the existence of a Frank-Kasper phase with hexagonal symmetry ($MgZn_2$ type, also labelled C14) in superlattices of monodisperse hydrophobically-coated gold particles (2 nm gold core diameter, hexanethiol as ligand) at room temperature, grown from suspensions in various volatile solvents. The existence of such a structure in this system has been analysed in terms of geometrical parameters including gold core diameter, ligand length and grafting density and an energetic approach based on van der Waals attraction[26].

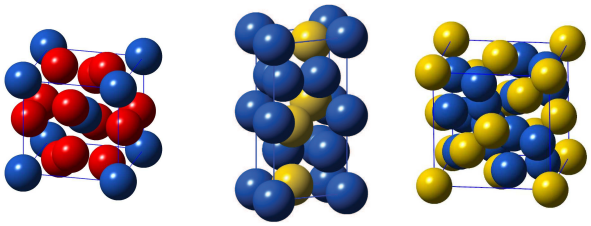

Figure 1 : Frank-Kasper structures: the A15 cubic phase (a), the C14 hexagonal phase (b) and the cubic C15 phase (c). The different colours in the A15, C14 and C15 structures correspond to sites with different coordination numbers Z: blue for Z=12, red for Z=14 and yellow for Z=16.

In this paper, we focus on the superlattice structures built by hydrophobically coated gold nanoparticles and we explore a large domain of sizes, varying both the core size and the ligand length. The aim of this work is to get more information on the role of the ratio L/R between the extended ligand length L and the core radius R. The gold NP self-assembly has been investigated for values of L/R close to 1, that is in the intermediate region between BCC and FCC structures. We report experimental results on superlattices built by nanoparticles with gold core diameters varying from 2 to 5 nm and coated with various ligands (from hexane-thiol to tetradecane-thiol). The ratio L/R has been varied from 0.6 to 1.8, in the region where the transition from a FCC structure to a BCC one is expected and where Frank-Kasper phases are suspected to be located.

2 Materials and Methods

All nanoparticles have been synthetized in our laboratory. The list of all samples prepared with about 30 different batches is detailed in †. Different synthesis have been used, all with alkane-thiols as ligands. The smallest particles (2 nm in diameter) have been synthetized using the Brust method[27]. The largest ones (4 to 5 nm in diameter) have been synthetized using the Stucky method[28]. To get gold nanoparticles with intermediate diameter, typically between 2.5 and 4 nm, we have performed a seeding-growth process starting from small nanoparticles (2 nm in diameter initially) as described in[28]. Different alkane-thiols have been used as ligands, from hexane-thiol to tetradecane-thiol. At the end of the reaction, the solvent is evaporated and ethanol is added to form a dark brown precipitate that is filtered off and washed with ethanol then dried. Organic solvents and the other chemicals were purchased from Sigma-Aldrich Co. and were used as received.

The nanoparticles (NPs) are then dispersed in oil. To perform a controlled self-assembly process, the NPs are dispersed in a volatile oil like toluene or cyclohexane at an intermediate weight fraction (typically 15 wt%). The suspensions are then stirred and sonicated before being poured in capillaries. Two types of capillaries are used, either cylindrical X-ray glass capillaries (diameter 1 mm, WJM glas@) or flat glass capillaries (Vitrocom@, 0.1 mm x 1 mm). The height of the capillaries is typically 10 cm and they are initially half-filled. The capillaries are sealed at one end and kept vertically to allow slow evaporation of the solvent by the top at room temperature. After several days, superlattices appear at the bottom of the capillaries but some can remain attached to the walls after drying of the solvent. For the same batch, several capillaries are prepared. Lower weight fraction suspensions (about 1 wt%) are also prepared in order to measure the gold core size and its polydispersity.

The size and polydispersity of the NPs have been determined by Small Angle X-ray Scattering (SAXS) performed on dilute suspension (about 1 wt%) in order to avoid interaction effects between the NPs and do the analysis using only their form factor term. This technique is a standard method to get the size and polydispersity with a very good statistics as a very large number of objects are averaged (typically 10^{12} NPs). However it is sensitive only to the gold cores. Indeed the ligands are much less rich in electrons than the gold cores and the contrast between the ligands and the solvent in terms of electronic density is too low. Data analysis has been done using a Schulz-Zimm distribution for the polydispersity and the NIST softwares[29]. The gold core polydispersity has been determined for all samples and is detailed in †: it is typically 15% for the smallest

particles (less than 3 nm in diameter) and 11% for the largest ones. The grafting density has been measured by thermogravity analysis (TGA) for part of the batches and was fully compatible with standard values[30], typically around 6 ligands *per* nm^2 for both synthesis.

The superlattice structure has been determined by SAXS. Many results have been obtained during the Run 20180220 on the Swing beamline of the synchrotron Soleil (France). The energy of the x-ray beam was 12 keV, and its wavelength was 1.0332 Å. The sample-detector distance was D=1.598 m and the size of the focused beam was typically 0.4mm (H)x0.1mm(V). The wave vector norm q is defined by $q = 4\pi \sin\theta/\lambda$ where 2θ is the angle between the scattered beam and the direct beam. The pixel detector (Eiger 4M, Dectris) is an assembly of several modules, with some gaps between them, as can be seen on the scattering patterns. All the capillaries have been scanned along the capillary axis and along its width, in order to obtain the best information and compare the structure and the cell parameter at different positions in each capillary or in different capillaries prepared with the same batch. The intensity scattered by superlattices is characterized by diffraction peaks depending on the structure, as described in †. If there are several superlattices with random orientation in the sample, these peaks appear as uniform circles at a given q position on the SAXS image. If the superlattices are not randomly distributed, the SAXS image exhibits spots located on these circles (textured pattern). For all patterns, the scattered intensity will be represented using a radial integration $I(q)$ at a given q value.

The information on the self-assembly structure is mainly extracted from the radial integration of the intensity, $I(q)$. For textured samples, only the position of the peaks (and not their intensity) gives reliable information. However, the detailed analysis of the scattering patterns shows that three other contributions have to be added to the superlattice structure contribution to describe more properly the measured intensity (see also details in †). At low q, the intensity increase can be explained by the presence of superlattice grains of small size giving a contribution that behaves as $I_1(q) \approx 1/q^4$, corresponding to the Porod scattering by their external surface. The other contribution is a diffuse peak whose maximum is located in the q region where the peaks have the strongest intensity. It can be interpreted as due to amorphous zones without any crystalline order between the nanoparticles. These disordered zones are expected to appear between the crystalline grains or could concentrate nanoparticules with dispersed diameter values. This contribution can be modelled using the structure factor $S_{HSS}(q)$ of a dense hard spheres assembly (Percus-Yevick analytical expression) characterized by the hard sphere radius R_{HSS} with a volume fraction close to 50%. This volume fraction roughly corresponds to the disorder-order transition for hard spheres. The last contribution is a background I_{bg} that has been taken as constant, independent of q. For a better comparison with the experimental radial intensity, a Debye-Waller attenuation ($\exp^{-q^2\delta^2}$) factor has been added to the peak intensities of the model in order to take into account the static or dynamic disorder. For the structure determination, only the diffraction peaks are considered. To visualize more easily the peaks, the experimental structure factor $S(q)$ for each pattern has been determined using $S(q) = \alpha(I(q) - I_{bgd})/FF(q)$ where $I(q)$ is the measured intensity, I_{bgd} is the background intensity assumed to be constant, $FF(q)$ is the form factor of the NPs and α is a constant scale parameter that fix $S(q) = 1$ when q is large. The graphs $S(q)$ as a function of q reveal the diffraction peaks more clearly (see †) even if the diffuse peak and the Porod domain scattering still contribute.

The different structures and their scattering properties are described in †. The smallest distance d between two NPs in each structure (nearest neighbour distance) is determined as follows. For a FCC structure, the cell is cubic (parameter a) and the space group is $Fm\bar{3}m$. The first diffraction peak corresponds to $q1_{FCC} = q_{111} = \sqrt{3}\ 2\pi/a$. The distance between neighboring particles is $d = a/\sqrt{2}$. For a BCC structure, the cell is cubic (parameter a) and the distance between neighboring particles is $d = a\sqrt{3}/2$. The space group is $Im\bar{3}m$. The first diffraction peak corresponds to $q1_{BCC} = q_{110} = \sqrt{2}\ 2\pi/a$. For a C14 structure, the cell is hexagonal (parameters a and $c = \sqrt{\frac{8}{3}}\ a$). The space group is $P6_3/mmc$. The first diffraction peak corresponds to $q1_{C14} = q_{100} = \frac{2}{\sqrt{3}} * 2\pi/a$ and the smallest distance between neighboring particles is $d = a/2$.

3 Results and Discussion

The main parameter that is expected to control the superlattice structure built by nanoparticles grafted wih soft ligands is the ratio L/R where L is the ligand length and R is the gold core radius of the particles assumed to be spherical. Here we consider for L the value of the fully extended ligand length as given by the Tanford formula

L (in nm)$=0.154+0.125*n$[31] where n is the number of carbon atoms in the ligand chain (Table 1). Note that this length is not the real shell thickness. However, the value of the fully extended chain is very useful in order to establish the effect of chain length.

Table 1 : Fully extended length in nm of n-alkanes.

n	6	7	8	9	10	11	12	14	16
L in nm	0.9	1	1.2	1.3	1.4	1.5	1.7	1.9	2.2

When the ratio L/R is small enough, that is typically smaller than 0.7, the NPs are expected to behave like "hard"' spheres and a FCC structure, driven by close packing, is observed. For large values of L/R, the ligand softness dominates and the structure is expected to be BCC. A C14 phase has been recently observed in the intermediate region and more precisely for a value of L/R close to 0.8[19]. The system exhibiting this C14 structure was 2 nm diameter gold core nanoparticles grafted with hexane-thiol. Such complex phase has been observed in many different soft systems as well as other tetrahedrally closed-packed structures. Understanding why these complex phases are observed is still under debate. For gold nanoparticles, the core is rigid and only the shell is soft. The aim of this work was to get more information on the role of L/R in the case of NP self assembly and to investigate gold NPs self-assembly for values of L/R close to 1, that is in the intermediate region between BCC and FCC structures. In order to carefully explore this region, the gold core diameter has been varied from 2 nm to 5 nm. Different alkane-thiol with various carbon atoms in the paraffinic chain (from 6 to 16 carbons) have been used. The extended length of hexane-thiol is 0.9 nm whereas that of tetradecane-thiol is 2.2 nm. More than 30 batches have been investigated. For each batch, several capillaries have been prepared and each capillary has been scanned with the X-ray beam. The structures have been determined using the best SAXS diffraction patterns.

For large values of L/R the BCC structure is observed as shown in Fig. 2a. For small values of the ratio L/R, the structure is FCC (Fig. 2b), as observed in many other experiments. When the ratio L/R is close to 1, the C14 structure appears (Fig. 2c). The C14 structure is quite easy to recognize. Its characteristic feature is a first group at small q of three diffraction peaks of middle intensity and located very close to each other at typically half value of that of the first diffraction peaks of the FCC or BCC phases. The location of these three peaks, indexed by (100), (002) and (101), is the signature of a larger unit cell for C14 than for FCC and BCC. The integrated intensity $I(q)$ with the peaks indexation is shown in Fig. 3 for the BCC phase, in Fig. 4 for the FCC phase and in Fig. 5 for the C14 phase. An important result is that the C14 structure is clearly observed for different core sizes and various ligand lengths. Indeed, the C14 phase is observed in the range $0.7 < L/R < 1.4$.

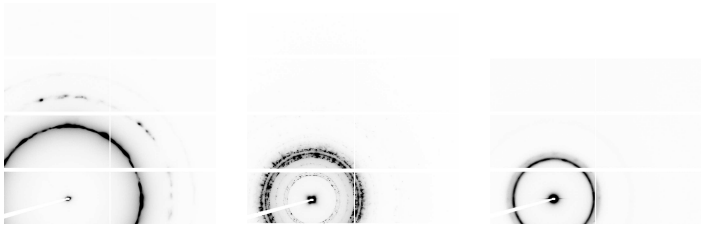

a) b) c)

Figure 2 : Diffraction patterns for a) BCC phase for L/R=1.6, b) C14 phase for L/R=1, c) FCC phase for L/R=0.7

The complete structure diagram as a function of L and R reveals to be rather complex. Indeed, in a large region intermediate between C14 and FCC, an additional strong and narrow diffraction peak is recorded close to the (110) peak of the C14 structure and can even sometimes be superimposed to it. We attribute the observation of this peak to the presence of another phase coexisting with the C14 phase. However, the identification of this coexisting phase is not possible when only one single extra peak is present. Fortunately, for some patterns, a more extended set of extra peaks that cannot be indexed with the C14 phase is clearly observed (Fig. 6).

Since the FCC phase is observed for slightly larger R/L values, one could suspect the coexistence of the

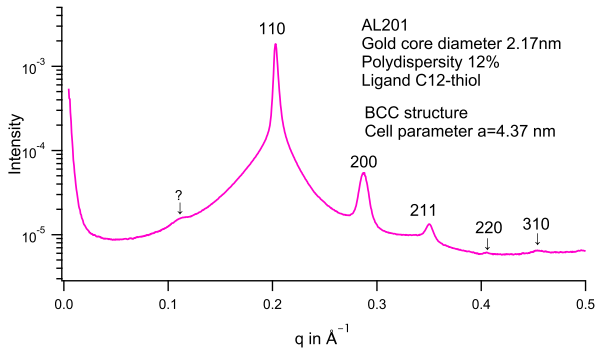

Figure 3 : Radial intensity $I(q)$ in arbitrary unit as a function of q in Å^{-1} typical of a BCC phase; L/R=1.6; (hkl) are indexed using a BCC lattice

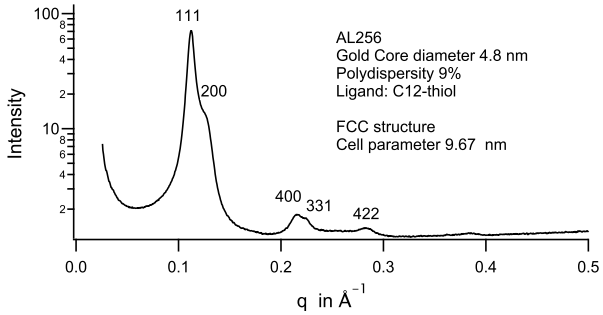

Figure 4 : Radial intensity $I(q)$ in arbitrary unit as a function of q in Å^{-1} typical of a FCC phase; L/R=0.7 (hkl) are indexed using a FCC lattice

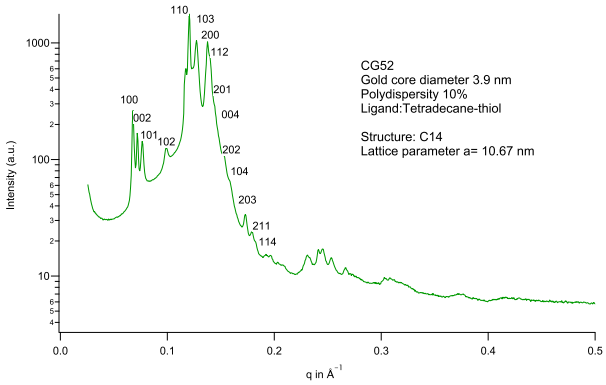

Figure 5 : Radial intensity $I(q)$ in arbitrary unit as a function of q in Å^{-1} typical of a C14 phase; L/R=1; (hkl) are indexed using a hexagonal lattice with $c = \sqrt{\frac{8}{3}}a$.

C14 with a FCC phase. If the first intense extra peak close to 0.12 Å^{-1} is attributed to a FCC (111) peak, the corresponding structure could be a FCC structure. The comparison of the experimental intensity with the intensity expected for a FCC phase is shown in Fig. 7. The unidentified peaks of Fig. 6 are in good agreement with a FCC phase with lattice parameter $a_{FCC} = 9.5$ nm and with a distance between neighboring particles 6.7 nm which is sligthly larger than in the C14 phase (5.3 nm). The weak intensity of the (220) FCC peak can be explained by the core form factor that is minimum around the corresponding q value. Other possible indexations than FCC have been tried and notably that of a C15 structure that is the cubic version of the hexagonal C14 phase[32]. For a coexistence between C14 and C15, mutual structural relationships are expected.

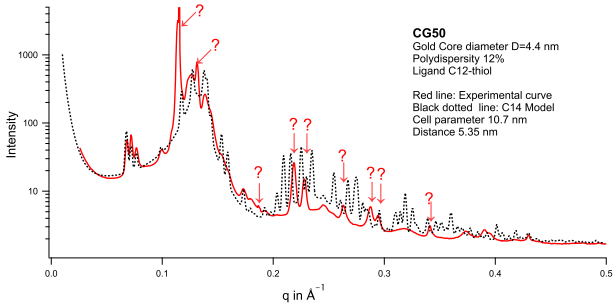

Figure 6 : Radial intensity $I(q)$ in arbitrary unit as a function of q in Å^{-1} with a clear evidence of a C14 phase (a_{C14}= 10.59 nm) in coexistence with another phase (Gold core diameter 4.4 nm, ligand C12-thiol). Comparison with the intensity expected for the C14 phase (black doted line) shows that some peaks (labeled with question mark symbol) cannot be indexed in the C14 structure indicating that another structure coexists with the C14 phase.

Indeed, the nearest neighbor distance between the particles would be the same and the C15 lattice parameter would therefore be $a_{C15} = 15.13$ nm $= \sqrt{2}a_{C14}$. In addition, the (111) peak would be located at the same position as the (002) peak of the C14 phase (same A3 symmetry axis). The comparison of the experimental intensity with the intensity expected for this C15 phase, presented in †, clearly shows that the source of this additional peaks cannot be due to a C15 phase or any phase related to the C14 phase by another stacking sequence like the C36 phase.

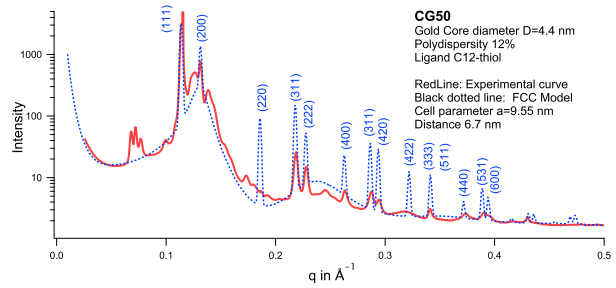

Figure 7 : Same data set as in Figure 6 compared with the intensity expected for a FCC phase (blue dotted line) in coexistence with the C14 phase. The unidentified peaks of Fig. 6 are in good agreement with a FCC phase with lattice parameter $a_{FCC} = 9.55$ nm.

The structures observed for different gold core diameters and thiol-ligands are presented in Fig. 8. The experimental structure diagram is represented as a function of the gold core radius R (horizontal axis) and of the number of carbon atoms in the alkane-thiol ligand. The two lines correspond to L/R=0.7 and L/R=1.4 where L is the fully extended ligand length. For L/R larger than 1.4, the structure is BCC. The FCC structure is observed for L/R smaller than 0.7. For intermediate values of L/R, the C14 phase is always observed, either as a single phase or in coexistence with another structure for the larger core size values ($R >$ nm). In the later case, some extra peaks with respect to the C14 peaks appear and they have been attributed to a FCC phase that coexists with the C14 phase (see Fig. 7).

Lastly, in one sample, another phase in coexistence with the C14 phase is observed and is clearly more complex than a FCC as shown in Fig. 9 for nanoparticles with diameter D=2nm and octane-thiol as ligand. The three diffraction peaks characteristic of the C14 phase are present but diffuse scattering close to the C14 peaks indicates the presence of stacking faults. Moreover another peak located at smaller q is visible, indicating the coexistence with another phase with a larger lattice parameter than the C14. This peak cannot be attributed to variants of the C14 phase with a larger c parameter like the C36 phase or another one with an even more complex stack sequence. Indeed, for such variants, the first peak along the c axis is located always at the same position, which is the (002) peak of the C14 phase (identical to the (111) peak of the C15 phase). The

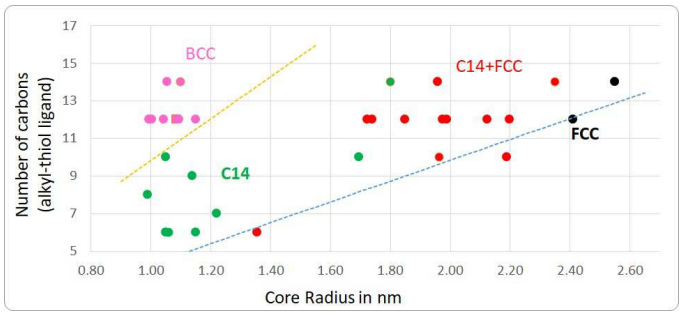

Figure 8 : Experimental structure diagram as a function of the gold core radius R (horizontal axis) and of the number of carbon atoms in the alkane-thiol ligand. The two lines correspond to L/R=0.7 and L/R=1.4 where L is the fully extended ligand length.

coexisting phase shown in Fig.9 has not yet been identified and is still under investigation. In conclusion, the experimental structure diagram (see Fig. 8) is certainly even more complex.

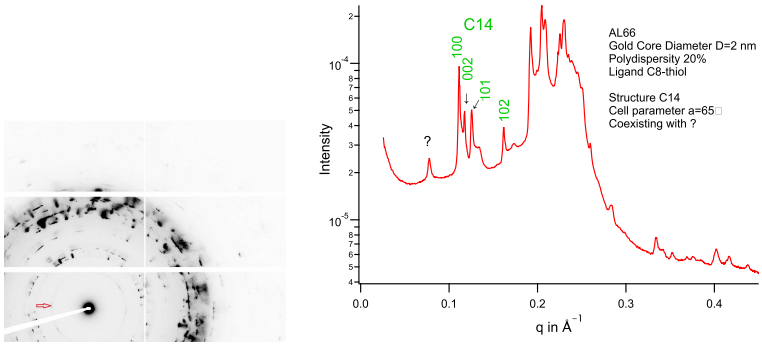

Figure 9 : Diffraction pattern observed for nanoparticles with gold core diameter D=2 nm grafted with octane-thiol ligands. An extra peak close to 0.078 Å^{-1} is clearly observed at q lower than the C14 peaks (indicated with a red arrow on the 2D image and a question-mark label on the intensity curve).

The coexistence of different ordered structures in polydisperse samples is not really surprising. It has already been discussed in[33] but it is the first time that it could be experimentally observed for colloids with a low polydispersity. However the role of the polydispersity on the phase diagram is still an open question. For gold nanoparticles, the core diameter is polydisperse, typically 10% or more, as measured on dilute samples by SAXS (see Table in †). A polydispersity in the grafting density cannot be excluded but is not easy to measure. The polydispersity could be different in the coexisting phases due to some partitioning of the nanoparticles. Even the classical BCC phase can coexist with another phase. For instance in the BCC pattern of Fig. 3, a small bump at q close to 0.1 Å^{-1} is the signature of another phase, probably C14. One can also notice that, in all patterns, a disordered phase contribution, with a bump close to the more intense peaks, is always superimposed with the structure Bragg peaks. This multiphase coexistence with at least one disordered phase has already been observed[16] in an electrostatic colloidal system and the existence of the C14 phase was interpreted as due to a partitioning inside the phase, linked with the occupied sites. In the same vein, the coexistence between a Frank-Kasper phase that is expected to require some polydispersity and the FCC phase or the BCC phase where all the sites are equivalent can be reasonably explained by some partition among the gold nanoparticles either involving either their core size or the ligand shell effective thickness. The coexistence of the C14 phase with a FCC phase may also be due to kinetics. We have already shown that, under evaporation, when the final phase is the BCC one, an intermediate FCC phase is observed[34]. This should also be the case for the C14 phase. But due to larger gold core volume fraction, part of the system could be kinetically trapped in the FCC phase and could not evolve to the thermodynamically stable C14 phase, leading to the coexistence between the two phases.

Different regions in the structure diagram can be delimited using the ratio L/R (see Fig. 8). But another important feature needs to be taken into account in the analysis of the phase diagram,that is the configuration of

the ligand conformation. Indeed the configuration of the ligands is not well known[35] and is expected to depend on many parameters as the ligand coverage, the facets or the temperature. The ligands can be more or less ordered and tilted or in a molten state. However, in all cases, the shell thickness is smaller than the extended length. Moreover, the chainsin-between two gold cores may be interdigitated . The ligand thickness in-between two neighbouring gold cores can give precious information on the ligand configuration. More precisely, the minimum thickness e of the soft region between the rigid gold cores can be computed as the difference between d, the minimum distance between neighboring particles (center to center), obtained from the cell parameter (†), and the mean gold core diameter $D = 2R$, obtained by SAXS on dilute suspensions: $e = d - D$. In Fig. 10, the e/L ratio is represented as a function of L/R for the different samples and the different structures. A table of the different values is given in †. The e/L ratio is close to 1 for the BCC structure, smaller than one for the C14 structure and larger than 1 for the FCC structure. In the literature, this ratio e/L for nanoparticles covered with dodecanethiol ligands varies between 1 and 1.8 in the FCC structure with some mean value around 1.3[36,37]. The results shown in this paper confirm these values.

Many-body effects must be taken into account to analyse nanocrystal superlattices[38]. The ratio between rigid core and soft corona has revealed to be a critical parameter to determine the self-assembled lattice[39]. Up to now, there are two main theoretical models proposed to evaluate the equilibrium distance between gold NPs. The optimal packing model (OPM) assumes that the ligands pack densely in the central part of the contact region between the two NPs. In that case, there is no or little interpenetration of the ligand shells and the particles behave as "hard" spheres. In this model, the thickness of the soft region between the particles is twice the thickness of the ligand shell. However the ligand shell thickness is expected to be lower than the fully extended ligand length L. Indeed, if the ligands are more or less ordered, they are expected to be tilted with respect to the surface normal[40], with a tilt angle around 40°. If the ligands are in a molten state, the shell thickness around each gold core is also smaller than the extended length. In both cases, the distance between the NP surface in the OPM model is thus expected to be smaller than $2L$ and the optimal packing model is compatible with the e/L ratio measured in the FCC phase. An alternative overlapped cone model (OCM) makes a proper assumption of dense ligand packing within the entire overlapping region for multi-particle system and no void in between the particles. The OCM model enables the prediction of the many-body effects and suggests a shorter NP-NP separation than the OPM model[41]. This is the case in the BCC phase and moreover in the C14 phase where the soft shells of neighbouring particles clearly interpenetrate. In the C14 phase, the particles are even closer with respect to the extended ligand length L that in the BCC phase. The ratio e/L remains close to 1 for the BCC phase but varies much for the C14 phase.

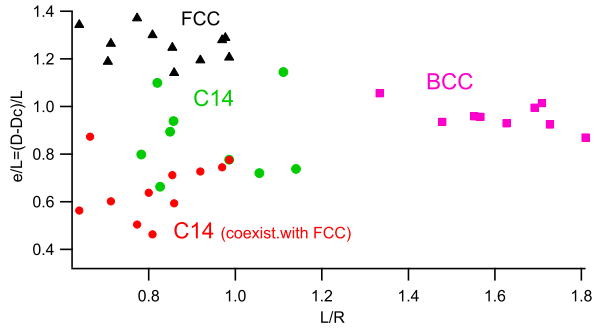

Figure 10 : The e/L ratio is plotted as a function of L/R for the FCC, BCC and C14 structures in different samples. The dispersion on the e/L is quite large ($\approx 50\%$ in the C14 phase).

The difference between the e/L ratio in the BCC phase and in the C14 phase can be justified by geometrical arguments, assuming that, in the BCC phase as in the C14 phase, the unit cell is totally filled by the soft particles with no void or solvent in between the particles. The mean volume per particle is then $\frac{1}{2}a_{BCC}^3$ in the BCC phase and $\frac{\sqrt{2}}{12}a_{C14}^3$. The smallest distance between neigbouring particles is $d_{BCC} = \frac{\sqrt{3}}{2}a_{BCC}$ in the BCC phase and $d_{C14} = \frac{1}{2}a_{C14}$ in the C14 phase. Assuming that the volume per particle is the same for both phase implies that $d_{C14} = (2/3)^{1/6}d_{BCC} \approx 0.93 d_{BCC}$. For the same mean volume per particle, the smallest distance between

neighbouring particles is smallest in the C14 phase than in the BCC phase as well as the ratio $e/L = \frac{d-D}{L}$. Simple computation leads to $\frac{e_{C14}}{L} = 0.93\frac{e_{BCC}}{L} - 0.07\frac{D}{L}$. Since the ratio $\frac{e_{BCC}}{L}$ is close to one, the ratio $\frac{e_{C14}}{L}$ is expected to be smaller than 1 and increases with increasing L/R ratio. This seems to be globally coherent with the behavior shown in Fig. 10. Still assuming that the cell is totally filled by the soft particles, one can notice that the volume fraction really occupied by the gold cores is typically less than 15% in the BCC structure, but higher in the C14 structure, up to more than 30%. The assumption of a total filling of the cell by the particles is roughly in agreement with the standard ligand coverage expected for these alkane thiol-grafted particles[30] (from 4.5 to 7 ligands per nm^2). The C14 structure is expected at larger gold core volume fractions compared to the BCC structure and for particles for which the soft corona deforms less easily. This could justify that, during evaporation, transforming a FCC phase into a C14 phase is more difficult than into a BCC one and could explain some kinetics effect on the experimentally observed structures.

The main results of this paper can be summarized in Fig. 11.

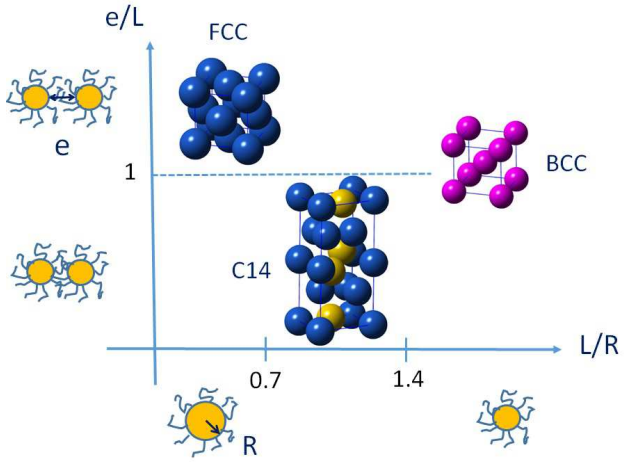

Figure 11 : Schematic representation of the structure diagram for soft gold nanoparticules with gold core radius R, covered by thiol-ligands with extended length L. e is the thickness of the soft medium between the gold cores. The C14 structure coexists with a FCC structure for the larger values of R.

4 Conclusions

Classical cubic phases are often observed in superlattices grown from suspensions of hydrophobically coated metallic nanoparticles: FCC when the soft coating thickness is thin compared to the rigid core radius or BCC when the soft coating thickness is large compared to the rigid core radius. In this paper we focus on the intermediate region between the BCC and FCC structures and establish an experimental structure diagram shown in Fig. 8. A large experimental investigation has been performed in order to carefully explore the effect of the core diameter from (2 nm to 5 nm) as well as the effect of the alkane-thiol length (from 6 to 16 carbon) on the nanoparticle self-assembly. In the intermediate region, a hexagonal Frank-Kasper C14 phase appears for different core sizes (radius R) and different ligands characterized by their fully extended length L. The region where the C14 structure is observed ranges typically from $L/R = 0.7$ to $L/R = 1.4$. These experimental results confirm that, as for other soft particles, Frank-Kasper phases are solutions to the problem of filling the space with hydrophobically-coated gold nanoparticles. Nevertheless the FCC phase coexists with the C14 phase in a large domain of the diagram. Several effects can explain this coexistence, such as polydispersity or kinetics. Some more complex phase with larger parameters than the C14 phase has also been detected, but not yet elucidated.

Our large experimental data set allows to quantify significant trends for key size ratios. For instance, the minimum distance e between the gold cores compared to the fully extended ligand length L depends on the structure: e is larger than L in the FCC structure, close to L in the BCC structure and smaller than L in the C14

Frank-Kasper phase. These experimental results should help to establish pertinent models in order to predict the structures of the superlattices built by gold nanoparticles.

For all samples, the crystalline phase of NPs coexists with at least one disordered phase. Multi-phase crystalline coexistence in the same sample is often observed, making the structural determination sometimes difficult. The ultimate structure diagram is certainly more complex since this study has revealed the existence of even larger unit cell structures. Understanding the origin of all these different complex phases for the hydrophobic gold nanoparticles remains a challenge. In this vein, the role of the NPs polydispersity as well as the ligand configuration is a recurrent question, but the self-assembly kinetics is also a key parameter.

Conflicts of interest

There are no conflicts to declare.

Acknowledgements

We acknowledge SOLEIL for provision of synchrotron radiation facilities and we thank Thomas Bizien for assistance in using beamline SWING. This work is funded by the French National Research Agency (SoftQC project; https://softqc.wordpress.com/; ANR grant ANR-18-CE09-0025). Pictures of the different structures have been made using CrystalMaker@ software by Jules Marcone during his internship.

References

[1] M. Grujicic, S. Tangrila, O. Cavin, W. Porter and C. Hubbard, *Materials Science and Engineering: A*, 1993, **160**, 37–48.

[2] F. Stein and A. Leineweber, *J. Mater. Sci*, 2021, **56**, 5321– 5427.

[3] B. Li, D. Zhou and Y. Han, *Nat. Rev. Mater.*, 2016, **1**, 15011.

[4] D. Weaire and R. Phelan, *Philos. Mag. Lett.*, 1994, **69**, 107–110.

[5] G. Shearman, A. Tyler, N. Brooks, R. Templer, O. Ces, R. Law and J. Seddon, *Liquid Crystals*, 2010, **37**, 679–694.

[6] C. M. Baez-Cotto and M. K. Mahanthappa, *ACS Nano*, 2018, **12**, 3226–3234.

[7] P. Ziherl and R. D. Kamien, *J. Phys. Chem. B*, 2001, **105**, 10147–10158.

[8] G. Ungar, Y. Liu, X. Zeng, V. Percec and W.-D. Cho, *Science*, 2003, **299**, 1208–1211.

[9] A. P. Lindsay, R. M. Lewis, B. Lee, A. J. Peterson, T. P. Lodge and F. S. Bates, *ACS Macro Letters*, 2020, **9**, 197–203.

[10] S. Lee, M. J. Bluemle and F. S. Bates, *Science*, 2010, **330**, 349–353.

[11] K. Kim, M. W. Schulze, A. Arora, R. M. Lewis, M. A. Hillmyer, K. D. Dorfman and F. S. Bates, *Science*, 2017, **356**, 520–523.

[12] A. J. Mueller, A. P. Lindsay, A. Jayaraman, T. P. Lodge, M. K. Mahanthappa and F. S. Bates, *ACS Macro Letters*, 2020, **9**, 576–582.

[13] T. M. Gillard, S. Lee and F. S. Bates, *Proceedings of the National Academy of Sciences*, 2016, **113**, 5167–5172.

[14] K. Yue, M. Huang, R. L. Marson, J. He, J. Huang, Z. Zhou, J. Wang, C. Liu, X. Yan, K. Wu, Z. Guo, H. Liu, W. Zhang, P. Ni, C. Wesdemiotis, W.-B. Zhang, S. C. Glotzer and S. Z. D. Cheng, *Proc. Natl Acad. Sci. U S A*, 2016, **113**, 14195.

[15] Z. Su, J. Huang, W. Shan, X.-Y. Yan, R. Zhang, T. Liu, Y. Liu, Q.-Y. Guo, F. Bian, X. Miao, M. Huang and S. Z. D. Cheng, *Nat. Chem.*, 2019, **11**, 899–905.

[16] B. Cabane, J. Li, F. Artzner, R. Botet, C. Labbez, G. Bareigts, M. Sztucki and L. Goehring, *Phys. Rev. Lett.*, 2016, **116**, 208001.

[17] B. W. Goodfellow, Y. Yu, C. A. Bosoy, D.-M. Smilgies and B. A. Korgel, *J. Phys. Chem. Lett.*, 2015, **6**, 2406–2412.

[18] B. W. Goodfellow, M. R. Rasch, C. M. Hessel, R. N. Patel, D.-M. Smilgies and B. A. Korgel, *Nano Lett.*, 2013, **13**, 5710–5714.

[19] S. Hajiw, B. Pansu and J.-F. Sadoc, *ACS Nano*, 2015, **9**, 8116–8121.

[20] E. V. Shevchenko, D. V. Talapin, N. A. Kotov, S. O'Brien and C. B. Murray, *Nature*, 2006, **439**, 55–59.

[21] A. Dong, J. Chen, P. M. Vora, J. M. Kikkawa and C. B. Murray, *Nature*, 2010, **466**, 474–477.

[22] X. Ye, C. Zhu, P. Ercius, S. N. Raja, B. He, M. R. Jones, M. R. Hauwiller, Y. Liu, T. Xu and A. P. Alivisatos, *Nat. Commun*, 2015, **6**, 10052.

[23] I. Coropceanu, M. A. Boles and D. V. Talapin, *J. Am. Chem. Soc.*, 2019, **141**, 5728–5740.

[24] A. Reddy, M. B. Buckley, A. Arora, F. S. Bates, K. D. Dorfman and G. M. Grason, *Proc. Natl Acad. Sci. U S A*, 2018, **115**, 10233–10238.

[25] A. Reddy and G. M. Grason, *Nat. Chem.*, 2019, **11**, 865–867.

[26] B. Pansu and J.-F. Sadoc, *Eur. Phys. J. E*, 2017, **40**, 102.

[27] M. Brust, J. Fink, D. Bethell, D. J. Schiffrin and C. Kiely, *J. Chem. Soc., Chem. Commun.*, 1995, 1655–1656.

[28] N. Zheng, J. Fan and G. D. Stucky, *J. Am. Chem. Soc.*, 2006, **128**, 6550–6551.

[29] S. R. Kline, *J. Appl. Crystallogr.*, 2006, **39**, 895–900.

[30] H. Hinterwirth, S. Kappel, T. Waitz, T. Prohaska, W. Lindner and M. Lämmerhofer, *ACS Nano*, 2013, **7**, 1129–1136.

[31] C. Tanford, *J. Phys. Chem.*, 1972, **76**, 3020–3024.

[32] C. M. Baez-Cotto and M. K. Mahanthappa, *ACS Nano*, 2018, **12**, 3226–3234.

[33] P. K. Bommineni, N. R. Varela-Rosales, M. Klement and M. Engel, *Phys. Rev. Lett.*, 2019, **122**, 128005.

[34] J. Schmitt, S. Hajiw, A. Lecchi, J. Degrouard, A. Salonen, M. Impéror-Clerc and B. Pansu, *The Journal of Physical Chemistry B*, 2016, **120**, 5759–5766.

[35] A. Widmer-Cooper and P. L. Geissler, *ACS Nano*, 2016, **10**, 1877–1887.

[36] S. I. Stoeva, B. L. V. Prasad, S. Uma, P. K. Stoimenov, V. Zaikovski, C. M. Sorensen and K. J. Klabunde, *J. Phys. Chem. B*, 2003, **107**, 7441–7448.

[37] N. Olichwer, T. Koschine, A. Meyer, W. Egger, K. Rätzke and T. Vossmeyer, *RSC Adv.*, 2016, **6**, 113163–113172.

[38] M. A. Boles and D. V. Talapin, *J. Am. Chem. Soc.*, 2015, **137**, 4494–4502.

[39] Z. Su, J. Huang, W. Shan, X.-Y. Yan, R. Zhang, T. Liu, Y. Liu, Q.-Y. Guo, F. Bian, X. Miao, M. Huang and S. Z. D. Cheng, *CCS Chem.*, 2020, **2**, 1434–1444.

[40] P. K. Ghorai and S. C. Glotzer, *J. Phys. Chem. C*, 2007, **111**, 15857–15862.

[41] P. Schapotschnikow and T. J. H. Vlugt, *J. Chem. Phys.*, 2009, **131**, 124705.